Treatment Planning Systems and Hadron Therapy Practice in France

Ludovic De Marzi, Annalisa Patriarca, Alejandro Mazal and Jean-Louis Habrand

1 Introduction

Radiotherapy, particularly particle therapy, is one of the main techniques used for the treatment of cancer today. The medical use of protons, with energies ranging from 60 to 250 MeV, is expanding all over the world, including in France. Since 1980, thousands of patients in France have been treated for a variety of different diseases by particle therapy. One neutron (1980–2007) and two proton (1991) facilities were opened in Orleans, Nice and Orsay, respectively. Early applications of protons concerned ophthalmological treatments (1991), followed by adult and paediatric intracranial or skull base tumours (1993), and then spine and sacrum sites (2012), while the use of neutron therapy stopped in about 2007. This experience gave rise to several carbon research or therapy projects in France (Lyon, Caen) as well as several other proton therapy projects. The first accelerators used for particle therapy were derived from facilities dedicated to nuclear physics research, mainly cyclotrons, synchrotrons or synchrocyclotrons. A clinical environment was then added to complement these installations: passive beam lines, treatment planning systems and dose algorithms were all developed in-house, before being commercially available. Scanning techniques will likely become the dominant proton or ion therapy modalities in the near future, and considerable attention has recently been paid to the development and improvement of physical models in dose calculation algorithms (still widely based on analytical approximations such as ray-tracing and pencil-beams), as well as in dosimetry equipment for quality assurance or commissioning. Due to their ballistic properties, small angular diffusion and precise depth dose distributions, protons and light ions allow highly conformational dose deposition and fairly good protec-

L. De Marzi (✉) · A. Patriarca · A. Mazal · J.-L. Habrand
Institut Curie – Centre de Protonthérapie d'Orsay, Paris, France
e-mail: ludovic.demarzi@curie.fr

J.-L. Habrand
Centre François Baclesse, Caen, France

A.V. Solov'yov (ed.), *Nanoscale Insights into Ion-Beam Cancer Therapy*,
DOI 10.1007/978-3-319-43030-0_14

tion of organ at risks. In turn, this type of therapy requires a more accurate planning system (submillimetric) for calculation of geometries and 3D dose distributions, for example using Monte Carlo methods.

This chapter will discuss the technical and clinical aspects of proton beam treatment planning, as many similarities exist between proton and ion therapy. This chapter includes a summary of the physics and approximations used in proton dose algorithms, including the impact of accelerator and nozzle modelling, a description of conventional delivery approaches such as passive scattering or pencil beam scanning, immobilization specificities and the need for accurate imaging of patient geometry. The issues of neutron generation, risk of second cancers, and radiobiological effectiveness (RBE) of protons will also be discussed. As several of these aspects are common to proton and ion therapy, one section of this chapter will be devoted to the differences between these techniques, especially the biological effects of radiation. Finally, recent developments and perspectives in the planning process will be presented.

2 Treatment Planning Process

The aim of treatment planning is to optimize and simulate dose distributions to a target volume and the surrounding normal tissues. This step is generally performed before the patient's first irradiation session, and allows prediction of treatment outcome based on the knowledge of specific dosimetric or biological parameters representative of local tumour control or probabilities of normal tissue complications. The treatment planning system (TPS) is software designed to perform these simulations and manipulate physical doses in order to deliver a uniform biological equivalent dose to the target volume, sparing the surrounding tissues as much as possible.

Several tasks are mandatory and strongly dependent in the treatment planning process. First of all, the patient's anatomy must be reconstructed in 3D.

2.1 Conversion of CT Information for Dose Calculation

Ion beam treatment planning is based on computed tomography (CT) imaging, acquired at kilovoltage X-ray energies. The information provided by CT images is used to account for attenuation and scattering of particle beams in dose calculations, and also to delineate target volumes and normal tissues. The relative ion stopping powers (stopping power ratio or SPR) in human tissues are deduced from Hounsfield units (HU) or CT numbers.

2.1.1 Principle

A commonly applied methodology to obtain an accurate relationship between HU values and SPR has been proposed for charged particle therapy [49, 63, 65]. This multistep stoichiometric calibration procedure has been described in the literature and is used to determine a tissue substitute calibration curve:

- A set of materials with known elemental composition and mass density close to tissue samples is scanned in the CT imaging system and the corresponding HU values are measured. Tissue samples are scanned individually in the centre of a water-equivalent phantom in order to ensure the same photon spectrum for each sample [63].
- The parameterization used for calculation of photon total attenuation coefficient ([36], Eq. 1) is defined from the known chemical composition and HU measurements of the tissue samples.
- This parameterization is used to compute the HU values of a selection of tissue samples and the SPR are calculated, for example from the Bethe Bloch equation for these tissue samples (Eq. 4).
- A final calibration curve (HU values vs. SPR) is fitted to the data: linear fits are calculated separately for adipose tissue, organ and muscle and bone categories, in order to divide the final curve into several segments (Fig. 1).

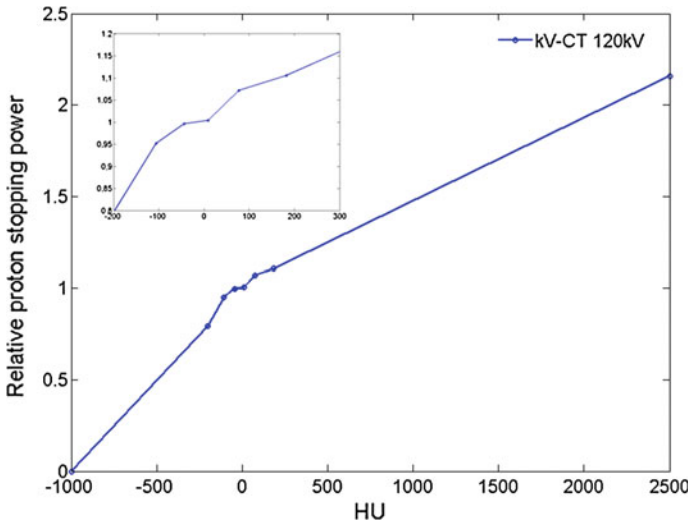

Fig. 1 Variation of relative proton stopping power as a function of HU values, for a 120 kV CT scan with a phantom diameter of 200 and 2 mm slice thickness. The *different lines* correspond to the linear fits to the biological tissues grouped into categories (adipose tissue, organ, muscle and bone)

Depending on the dose calculation model, the calibration curves (HU values vs. SPR or mass density) are then stored in the treatment planning system database for each CT scanner protocol. An internal material list, typically composed of a few dozen materials, mass densities, elemental composition and mean ionization energy, is used to associate HU values with material properties for each voxel of CT images. CT conversion methods have also been applied to Monte Carlo (MC) dose calculations, essentially based on conversion to mass density and elemental composition assigned to materials rather than water equivalent properties [40, 66, 76].

2.1.2 Basic Equations

Total Attenuation Coefficient

For a mixture of elements, the total attenuation coefficient μ can be obtained in the "Jackson and Hawkes" form [36], using Rutherford's parameterized cross-section of scattering processes:

$$\mu = \rho N_g(Z, A)\left\{K^{ph}Z_1^{3.62} + K^{coh}Z_2^{1.86} + K^{KN}\right\} \tag{1}$$

where ρN_g is the electron density and K^{ph}, K^{coh} and K^{KN} are constants that characterize the cross-sections of the photoelectric effect, coherent scattering and the cross-section of Klein Nishina, respectively. These constants are dependent on the scan technique used, and parameterize the response of the CT scanner. N_g, Z_1, Z_2, and λ_i are given by:

$$N_g = \sum_i N_g^i = N_A \sum_i \frac{w_i Z_i}{A_i} \tag{2}$$

$$Z_1 = \left[\sum_i \lambda_i Z_i^{3.62}\right]^{1/3.62} \quad Z_2 = \left[\sum_i \lambda_i Z_i^{1,86}\right]^{1/1,86} \quad \lambda_i = \frac{N_g^i}{N_g} \tag{3}$$

where $N_A$is Avogadro's number, Z_i is the atomic number, A_i is the atomic weight of the *i*th element

Relative Proton Stopping Power in Human Tissues

The relative mass stopping power can be calculated for human tissues, based on the Bethe-Bloch equation [65]:

$$SP_w^m = \frac{\rho_e^m \rho^w}{\rho_e^w \rho^m} \frac{\left\{\ln\left[2m_e c^2 \beta^2 / I^m (1-\beta^2)\right] - \beta^2\right\}}{\left\{\ln\left[2m_e c^2 \beta^2 / I^w (1-\beta^2)\right] - \beta^2\right\}} \tag{4}$$

where β = v/c is the 'normalized' velocity (*v* the projectile's velocity, *c* the speed of light), m_e is the electron mass and $I^{m,w}$ are the mean ionization energies of atoms for medium and water. The value of $\ln(I^m)$ for a mixture can be calculated using the Bragg additivity rule:

$$\ln(I^{m}) = \left(\sum_{i} \frac{w_i Z_i}{A_i} \ln I_i\right)\left(\sum_{i} \frac{w_i Z_i}{A_i}\right)^{-1} \tag{5}$$

with $Z_{i,}$ A_i Ii and w_i atomic number, atomic weight, ionization energy and percentage contribution by weight of *i*th element i in tissue, respectively. The relative electron density of medium to water can be calculated using:

$$\frac{\rho_e^m \rho^w}{\rho_e^w \rho^m} = \frac{N_g^m}{N_g^{eau}} \tag{6}$$

where ρ is the mass density and N_g is the number of electrons per unit volume defined in Eq. (2).

2.1.3 Uncertainties and Perspectives

Potential errors in the prediction of beam range in patients, derived from the conversion process, noise and partial volume effects in images, metallic implants or beam hardening artifacts, were estimated to be between 1–3 mm [48]. The approximation of relative biological effectiveness values in clinical practice and underestimation of its value at the end of the Bragg peak (also see an example Fig. 7) can generate an extension of the biological range of the order of 1 mm [53]. Moreover, different values have been obtained for the ionization energy of water, typically estimated to be around 75 eV that can lead to uncertainties in the depth of the Bragg peak by up to several millimetres [1].

Consequently, in practice, the gradient at the distal end of particle dose distributions is also rarely used (or used for a small fraction of the total dose) to spare critical normal tissues due to uncertainties about their exact position, and safety margins proportional to a few % of the range are added to the planning target volume (PTV). Recently, dual energy (DE) or megavoltage (MV) computed tomography has been investigated in order to improve elemental mass fraction predictions, potentially mitigate beam hardening and metal artifacts which limits the accuracy of kV-CT [13]. Photon attenuation is strongly dependent on the energy spectrum used and can vary with the size of the phantom and the position of the heterogeneity, and metallic implants induce artifacts leading to inaccuracies in the calculated ion beam range.

Moreover, several alternatives are also being explored to manage range uncertainty: proton tomography is being investigated by several teams as a means to improve treatment planning in terms of range and dose deposition predictions. The use of proton imaging could provide supplementary information on the stoichiometric composition of the tissues and cross-sections for nuclear interactions and could reduce uncertainties in the final proton range [4, 12]. Proton radiography is also expected to achieve submillimetric spatial resolution with low imaging dose deposition to the patient, for example when using a filtered-backprojection reconstruction algorithm with estimation of the most likely path of protons [57]. Finally, evaluation

of tissue activation or detection of prompt gamma rays produced by nuclear interactions [24, 39, 43] could lead to an in vivo estimation of the position of each individual Bragg peak delivered during the treatment session. Visualization and quantification (offline and/or online) of carbon-11, oxygen-15 isotopes or prompt gamma emission produced in the patient before the beam stops has been made possible by the use of new PET, single- or multiple-slit cameras in or adjacent to the treatment room.

2.2 Segmentation

Structure segmentation constitutes a second step in the treatment planning process. In this task, the tumour and volumes (Planning Target Volume—PTV), organs at risk (OAR) and other structures are defined, for example according to the published recommendations for prescribing, recording and reporting radiation treatments (for example ICRU report 78, addressing proton beam therapy). This task, similar to segmentation in standard 3D conformal radiation therapy, is generally performed with conventional segmentation software and has no specific characteristics in particle therapy, one of the several treatment modalities that will benefit from recent software developments in terms of deformable registration and dose accumulation.

2.3 Dose Calculation Algorithms

The next steps in the treatment planning process consist of definition and optimization of treatment parameters and calculation of the resulting dose distributions. A few definitions, useful for a better understanding of dose calculation algorithms without discussing the details of analytical models, are presented below.

2.3.1 Proton Beam Algorithms

Range-Energy Relationship, Bragg Peak Model

Assuming a continuous slowing down approximation (CDSA), i.e. the range of a particle is given by integrating the total stopping power from 0 to the initial energy, a power law relationship known as the Bragg-Kleeman rule describes the range-energy relationship of the particle. For therapeutic protons in water with E_0 <200 MeV (see Eq. 7), the power p and the factor α have been determined based on ICRU 49 by p = 1.77 and $\alpha = 2.2 \times 10^{-3}$ [5].

$$R_0 = \alpha E_0^p \tag{7}$$

This equation can be used to derive an analytical model of the Bragg curve [5], which includes an empirical model of nuclear fragmentation (primary fluence reduc-

tion due to nuclear interactions) based on data fitting, energy spread of polyenergetic beams (Eq. 8), which accounts for range straggling distribution with depth z caused by the statistical fluctuation in the energy loss process (Eq. 9).

$$\hat{D}(z) = \phi_0 \frac{(R_0 - z)^{1/p-1} + (\beta + \gamma\beta p)(R_0 - z)^{1/p}}{\varsigma p \alpha^{1/p}(1 + \beta R_0)} + \varepsilon\phi_0 \frac{(R_0 - z)^{1/p}}{\varsigma \alpha^{1/p} R_0 (1 + \beta R_0)} \quad \text{for } z \leq R_0 - 10\sigma \tag{8}$$

$$D(z) = \frac{1}{\sqrt{2\pi}\sigma} \int_0^{R_0} \hat{D}(z) \times e^{\frac{-(z-\bar{z})^2}{2\sigma^2}} d\bar{z} \qquad \text{for } R_0 - 10\sigma < z < R_0 + 5\sigma \tag{9}$$

where R_0, ϕ_0, σ and ε are nominal range, primary fluence, standard deviation of the Gaussian distribution and fraction of the primary fluence contributing to the 'tail' of the energy spectrum, respectively. This type of model, sometimes modified with a combination of parabolic functions of R_0 [82], can easily be simultaneously fitted to experimental data with sufficient accuracy to allow interpolation from data and to be used in dose calculation algorithms for routine treatment planning.

Ray-Tracing Algorithm

Accurate dose algorithms must include models for the sharp lateral penumbra and the rapid fall-off of the dose of protons or light ion beams. Fast broad-beam versions of such algorithms, giving accurate results for penumbra calculation, were first developed and based on ray-tracing techniques applied to CT images. The dose to a point of interest P with coordinates (X, Y, Z) is obtained from water-equivalent depth calculations (based on CT images information) and linear interpolation of reference depth dose curves measured in a water phantom. However, ray-tracing algorithms usually do not fully take into account straggling effects emerging from complex inhomogeneities, body surface irregularities, lateral spreading of the beam from beam-modifying devices upstream of the patient such as apertures and compensators. To achieve better modelling of the collimator edge effects, a lateral dose profile of a broad beam was therefore defined as the product of a central axis dose and a beam profile function [42]. This lateral dose profile function can model the radial distribution of protons induced by multiple Coulomb scattering through the media along the beam path, particularly scattering of the beamline elements and within the patient. A semi-experimental method was subsequently developed [51] to determine the beamline contribution from lateral penumbra measurements in air, and to take into account complex apertures using a sector integration method for irregular fields based on the Clarkson and Cunningham algorithm.

Pencil Beam Algorithm

As broad beam algorithms do not fully take into account internal inhomogeneities in the patient, the most commonly applied dose calculation algorithm for particle therapy is pencil beam. For example, in most models, the proton pencil beam algorithm factorizes into a depth-dependent term, proportional to the central axis depth dose curve for a broad beam, and a lateral fluence distribution that includes the effect of multiple Coulomb scattering. The lateral fluence distribution is usually decomposed

into a large number of small pencil beams, whose parameters are scaled to model the effects of media heterogeneities. In the case of pencil beam scanning (i.e. beam delivery system), the same algorithm is used but modified as a discrete summation.

The central axis depth-dose curve can be described by analytical approximations ([5], Eqs. 8, 9), taken from measurements or from theoretical calculations [74]. The lateral fluence distribution for any pencil beam can, at first approximation, be analytically described by a Gaussian shape with a standard deviation σ or small angles, but deviates from the Gaussian shape for larger angles (an accurate multiple Coulomb scattering theory was developed by Molière in 1948). Empirical formulae and parameterizations based on a theoretical background were then described to predict σ as a function of beam energy and depth in media [19, 32, 33]. An experimental procedure for the determination and verification of the parameters used in a proton pencil beam algorithm has been presented [71], as well as approximations that may be used for the lateral fluence distribution, beam energy modulation and lateral penumbra in the presence of compensators. An improvement of the algorithm for heterogeneous slab geometries and based on an additional 2D scaling of the lateral proton fluence was then described [72], and was further generalized to any heterogeneous geometry and scattering power model [80].

The first component of the lateral fluence distribution is then described analytically, based on a two-dimensional symmetric Gaussian function, given by Eqs. (10) and (11):

$$D_1(X, Y, Z) = D(Z) \times \frac{1}{\left(2\pi\sigma(Z)^2\right)} \exp\left(\frac{-\left[(X - X_0)^2 + (Y - Y_0)^2\right]}{2\sigma(Z)^2}\right) \tag{10}$$

$$\sigma(z)^2 = \sigma_{beamline}(z)^2 + \sigma_{tissue}(z)^2 \tag{11}$$

where (X_0, Y_0) are the coordinates of the pencil beam axis, σ escribes the total lateral spread of the beam, $\sigma_{beamline}$ and σ_{tissue} account for the beamline dependent scattering and multiple Coulomb scattering within the tissue at depth z, respectively.

Dose Algorithms for Scanned Pencil Beams

In high-energy particle beams, nuclear reactions are responsible for removal of primary particles from the incident beam, as well as production of fragment particles, resulting in a tail of the beam lateral dose distribution at more than three standard widths away from the central axis. As shown in Fig. 2, the main reaction products for a proton pencil beam are secondary protons, including alphas and deuterons. The most important dose contributions are those from secondary protons (as much as 10 % of the total dose).

The effects of these large-angle scattered fragments (produced by nuclear interactions) or large angle Coulomb scattering of primary particles on the physical dose distribution are accounted for in treatment planning systems by a sum of Gaussians fitted with measured or simulated data. As proposed by several authors [55, 69] for protons, the transverse dose profile of a scanned particle beam is modelled as the superimposition of at least two Gaussian distributions. In this model (see Eq. 12),

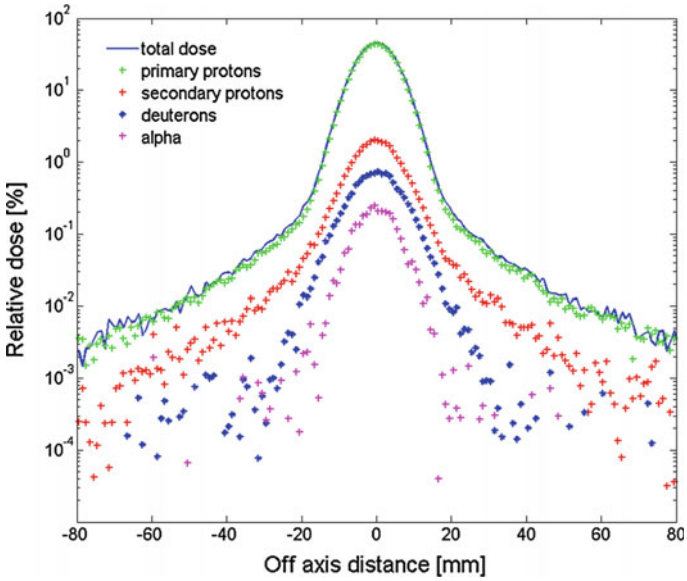

Fig. 2 Lateral profile of a pristine 160 MeV proton beam (sigma in air of 5 mm) in water at mid-range (at depth = 8.5 cm) showing the transverse dose distribution for different secondary components. Data are from GEANT4.9.3/GATE6.2 simulations

the first Gaussian component (G_1) describes the primary particles, whereas the second component (G_2) describes the beam halo from large angle scattered particles. Figure 3 presents an example of comparison between Monte Carlo simulated data and calculations based on a three Gaussians parameterization (from TPS ISOgray, Dosisoft).

As the exact extent of nuclear contribution at large scattering angles is not properly validated by calculation models nor separately accessible by measurements, several analytical approximations or fitting procedures have been described to determine the weight w and functional form of the second component in Eq. (12) for proton beams [69] or ions [34, 68]. Different parameterizations based on accurate measurement for a 177 MeV proton beam and description of the distinct components from a physics point of view have also recently been proposed [20].

$$D(X, Y, Z) \equiv D(Z) \times [(1 - w)\, G_1(X, Y, Z) + wG_2(X, Y, Z)] \qquad (12)$$

Monte Carlo Simulations

However, fast analytical algorithms present several limitations in terms of accuracy of calculation and more accurate dose calculation codes are needed, for example in very heterogeneous geometries where the effects of diffusion might be excessively smoothed and hot or cold spots may be underestimated. Monte Carlo dose calculations are considered to be the most accurate method to compute doses in radi-

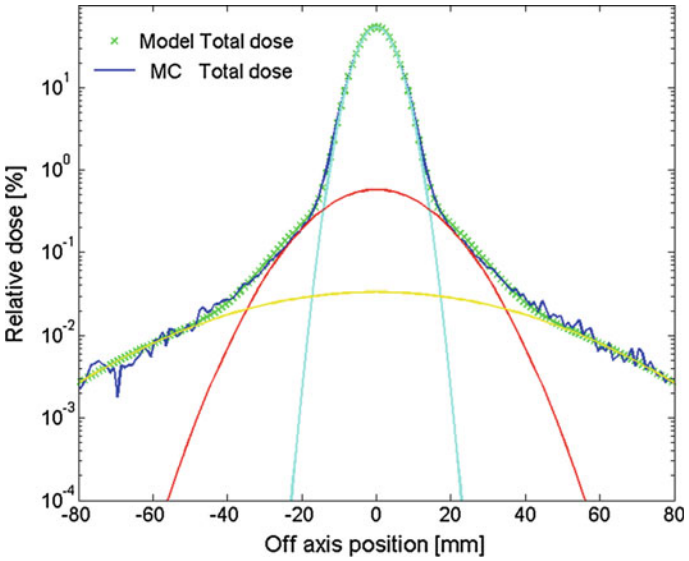

Fig. 3 Lateral profile of a pristine 180 MeV proton beam (sigma in air of 4 mm) in water at mid-range (at depth = 10 cm) showing the transverse dose distribution: simulated data from GEANT4.9.3/GATE6.2 (*solid line*), model with a superimposition of three Gaussians (*crosses*). The contributions of the different terms in the fit are also shown

ation therapy, as Monte Carlo simulations take into account the physics of particle interactions on a particle-by-particle basis using theoretical models or experimental cross-section data for electromagnetic as well as nuclear interactions. Monte Carlo dose calculations also consider tissue inhomogeneities by using material properties, atomic elemental composition, electron density, mass density or ionization potential, and secondary particle tracking. The main advantages of these codes in radiation therapy are that they can be used as references for validation purposes, for simulations of the components of the treatment head and to extract parameterized phase spaces for complex beam delivery systems. They can also validate or be used for the commissioning of beam delivery systems, and the quality assurance of clinical beam delivery. Therefore, although the main well-known Monte Carlo codes (MCNPX, GEANT4, and FLUKA) were initially designed for simulations in particle and nuclear physics, all of them have been successfully used in the field of particle therapy, as illustrated by the following examples.

In the framework of research studies, the Centre Antoine Lacassagne installation has been modelled in MCNPX [30, 31] to provide absolute dosimetry and independent monitor unit calculations for ophthalmological proton beam therapy. Also with MCNPX, a partnership between several French teams (Institut Curie, CEA/IRFU, IRSN) has led to the modelling of all Institut Curie passive beam lines [61, 70], and extensive comparisons of proton and neutron dose calculations versus experimental measurements have been performed. The MCS algorithm of MCNPX was modified

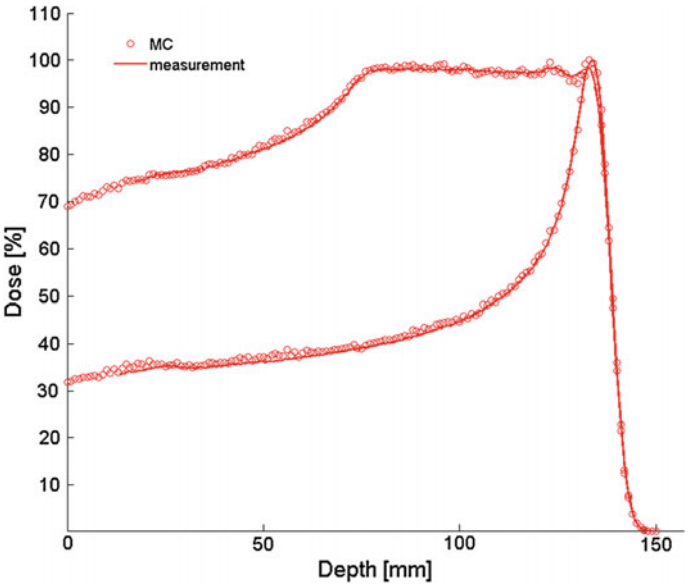

Fig. 4 Comparison of central axis depth dose in water (120 mm diameter field, 140 MeV SOBP and pristine Bragg peak). Data are from CC13 ionization chamber measurements (*solid line*) and GEANT4/GATE MC simulation (*circle*)

in order to improve the modelling of multiple Coulomb scattering in the case of thin foils [70].

GATE (Geant4 Application for Emission Tomography) is an advanced and versatile open source software, which contains tools dedicated to radiotherapy applications [37, 38, 60]. A Monte Carlo simulation of the IBA active scanning system with this platform, a reference physics list and a list of optimized parameters have been proposed for proton therapy [21–23]. An example of calculation using this platform is shown in Fig. 4 for a spread-out Bragg peak (SOBP) of a passive beam line.

In the framework of nuclear imaging for hadron therapy monitoring, nuclear models implemented in GEANT4/GATE and FLUKA were compared for monoenergetic protons and carbon ions, showing discrepancies between the two codes in terms of the spatial and time distributions of secondary particles [58].

Until very recently, Monte Carlo dose calculation, including treatment head simulation and dose calculation for passive scattering or beam scanning delivery were not commercially available. The main challenges for fast and reliable MC codes are to decrease the computer calculation time, while maintaining reliability, and to provide users with tools for automatic conversion of HU values, DICOM RT-ION and 3D dose or phase space outputs. Consequently in collaboration with several French teams (CEA/LIST, Institut Curie, DOSisoft, Centre Antoine Lacassagne, CEA/IRFU, INSA Lyon), a code (called PROUESSE) based on the Monte Carlo code PENELOPE [59] has been developed for proton-induced dose calculations and is currently in the process of validation. Furthermore, parallel architecture, for example based on

graphical processing units (GPU), is now very frequently addressed in new versions of Monte Carlo codes [3] or dose calculation engines in TPS, opening the way for four-dimensional or real-time treatment planning.

3 Beam Delivery Techniques

Three main delivery techniques are used in particle therapy. One is called passive or double scattering (DS) and consists of producing a broad beam, and is the delivery technique most commonly used worldwide. The two other delivery techniques are called uniform (US) and pencil beam scanning (PBS) and consist of magnetically scanning several pencil beams over the target volume, with the possibility of modulating the path, energy and intensity of the beams.

3.1 Passive Scattering Technique

To achieve the necessary uniformity of the radiation field required for clinical treatments (within a few percent), many methods for lateral spreading of particle beams have been investigated. The passive systems, composed of single or double scatterers, are one of the main techniques used to achieve conformal beams [50]. In a double scattering beam line, the dose is delivered with good conformity to the lateral and distal edges, but not to the proximal edge of the tumour. For this purpose, the range of different Bragg Peaks is adjusted with a range-shifter, while a second scatterer laterally enlarges the beam size. A dynamic wheel (e.g. aluminium propeller), that can be synchronized to the beam source in each case, is used to adjust the modulation value (a characteristic spread-out Bragg peak is shown in Fig. 4). Sets of collimators along the beam line limit secondaries, and divergent brass collimators, personalized to each patient, are used to obtain a smaller lateral penumbra at the end of the beamline. A range-compensator is used to achieve accurate distal target dose conformation. For example, at Institut Curie, compensators are made of Lucite blocks, manufactured with a computer-controlled drilling machine according to the target volume and each individual patient's anatomical data. Patients are usually preferably treated in the horizontal position, immobilized on a patient table, but sometimes in supine, prone or seated positions. To irradiate patients with all degrees of freedom, patient supports are usually mounted on robotic arms, which allow rotations and translations with few angular restrictions [47].

3.2 Uniform Scanning

The Uniform Scanning systems (for example those of IBA for proton beams) can deliver uniform transverse dose distributions up to 40x30 cm^2 treatment area. The

beam is scanned continuously according to a predefined scanning pattern. Two perpendicular dipole magnets scan a large spot along a fixed pattern at a constant frequency. The optimal beam spot size is determined by the system to achieve the required field size and uniformity for all layers. The scanning amplitude is also related to the field size and beam diameter: the scanning area is defined as the uncollimated proton field projected at the isocentre plane. Patient-specific apertures and range compensators are used to laterally and distally shape the radiation field appropriate for treatment. Minor, if any, modifications of the treatment planning system dose calculation algorithms are assumed from double scattering to uniform scanning. Indeed, the main differences between US and DS concern the transverse characteristics and absolute values of lateral penumbras, usually customizable in the TPS beam data library. The uniform scanning method also has a few advantages over passive beam delivery systems, mainly due to a smaller thickness of scattering material, as the transverse and distal penumbra widths show a slight improvement in comparison to those achieved with scattered beams for an equivalent field size. The maximum field size, the maximal range in water as well as the modulation width of a spread-out Bragg peak (SOBP) can also be slightly increased at a given accelerator energy.

3.3 Pencil Beam Scanning

With intensity-modulated particle therapy (IMPT) techniques, a narrow pencil beam is scanned magnetically over the target volume, while both the energy and the intensity of the beam are modulated: pristine Bragg peaks of a few millimetres are obtained and can be scanned transversally at average speed of a few m/s. Between two spot irradiations, the beam is usually turned off during magnet and energy modifications. Just as IMRT with photons led to vast improvements in conventional radiotherapy, simulations show that IMPT can provide significant improvements and much more conformal dose distributions. For IMPT, a discrete fluence map is optimized and converted into a set of continuous time-functions describing the beam position and current required for continuous beam scanning.

Two methods can be used for intensity-modulated proton therapy: the first is called single field uniform dose (SFUD) and the second one is called intensity-modulated proton therapy (IMPT). In SFUD, the extent of the spread-out Bragg peak is matched to the thickness of the target volume on each pencil beam axis. The modulation of the pencil beams is limited in the transverse plane in order to minimize the proximal dose to the target volume and to maintain a uniform dose distribution in the tumour. With the IMPT technique, Bragg peaks are distributed in three dimensions throughout the volume with free optimization of the intensity of each individual Bragg peak. As shown in Fig. 5, the definition of spot geometry and assignment of initial weights depend on the optimization procedure and must take into account accurate beam modelling to ensure correct coverage of the target.

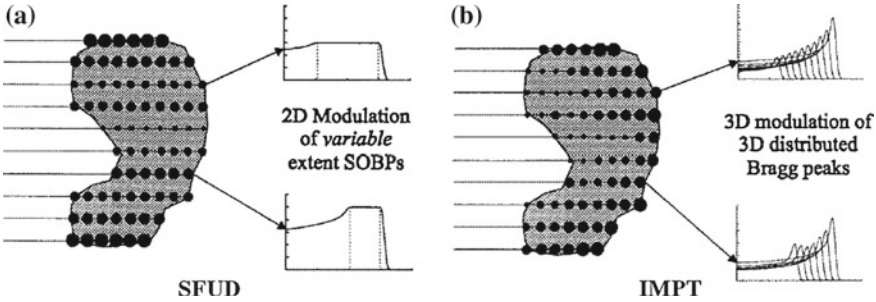

Fig. 5 Diagrams and representative depth-dose curves for **a** SFUD and **b** IMPT approaches to pencil beam scanning proton therapy (from [44])

4 Treatment Plan Optimization

Many special issues in treatment planning optimization for particle therapy are currently being addressed: multi-criteria optimization, sensitivity to the delivery uncertainties for inhomogeneous fields, radiobiological effects that can be included in pencil-beam based inverse optimization (through linear energy transfer (LET) calculations). The degeneracy of solutions in treatment planning can be used to incorporate management of uncertainties, especially in the optimization process. However, optimization techniques differ between the main beam delivery methods (i.e. passively scattered and scanned beams). With the double-scattering technique, optimization is based on manual operations and a set of practices and tools. For example, some of the following parameters can be adjusted: the compensator can be enlarged to guarantee target coverage even in the presence of small misalignments, narrow target extensions, or internal organ motion, the beam angles can be optimized to minimize or avoid consequences from high-gradient changes in density (bone-air) and reduce integral dose to healthy tissues, beams that pass through metal implants can be avoided because of range uncertainties associated with artefact in images especially near critical structures, and field overlapping on skin is usually also minimized. Treatment angles are also selected manually (only a few beams are usually used in pencil beam scanning or ion therapy, as dose conformation is excellent), sometimes with the help of accurate 3D visualizations available in TPS. Intensity-modulated particle therapy, made possible by pencil beam scanning, is based on inverse planning and can lead to significant improvements in particle therapy [44]. A discrete fluence map is optimized by the treatment planning system, and is converted into a set of beam weights. The optimization problem is based on the minimization of the cost function that expresses the difference between the planned dose D_0 and the calculated dose D_j (Eq. 13) for the set of beam weights w (Eq. 14). Iterative algorithms are used to find the solution of this problem, which reflects the physician's requirements by the use of dose-volume constraints and objectives.

There is a linear relationship between the dose D_j to the point of calculation j and the beam weights w_i:

$$D_j(x, y, z) = \sum_i w_i \times D_{ij}(x, y, z) \tag{13}$$

where D_{ij} is the dose contribution of pencil beam i to the point of calculation j.

$$w = [w_i] = \min_w \left\{ \sum_{j \in structure} g_{j^2} \times \left(D_j(x, y, z) - D_0\right)^2 \right\} \tag{14}$$

where g_j is the importance factor to the point of calculation j.

The problem in Eq. (14) can be reduced to solving a quadratic equation. Boundary conditions have to be added to take into account the non-negativity or minimum constraints for beam weights (for example, depending on the machine, there is a minimum value for monitor units and beam-on time), and possibly constraints on calculated doses for certain points. The projected conjugate gradient with penalties is a relevant algorithm for such problems and is implemented in some TPS (ISOgray, Dosisoft).

4.1 Robustness

Range uncertainties constitute the most significant risk in particle therapy, and may be initially managed by applying margins that expand the distal target volume (the current standard is to use linear scaling of stopping power and apply a range-uncertainty margin of ≈3 % + 1 mm). However, this approach does not guarantee robustness of the treatment plan, as uncertainties may combine and distort the dose in a non-linear way.

Table 1 Indicative overview of strengths (+) and weaknesses (−) of the various beam delivery techniques, as these parameters may vary according to acceleration type and optimization algorithms

	DS	US	SFUD	3D-IMPT
Optimization	No	No	Single-field	Multi-field
Homogeneity	Yes	Yes	Yes	no
Integrated boost	No	No	No	yes
Robustness (setup errors)	−	−	+	+
Robustness (motion errors)	+	+	−	−
Target size	−	+	+	+
Treatment time	++	+	−	-
Neutron contamination	−	+	++	++
Conformity	−	+	+	++

Various other approaches to ensure robust IMPT have been investigated by different teams worldwide: the "worst case scenario" [45] selects the best plan, while considering minimum and maximum doses in the target and healthy volumes for a limited number of range errors and shifted positioning scenarios. This strategy was subsequently refined assuming prior knowledge of the probability distribution of the uncertainty [75]. A multi-criteria optimization (MCO) framework has also been introduced to investigate the trade-offs between conformity and robustness when selecting clinically achievable plans [9] (Table 1).

5 Clinical Aspects and Status

The clinical experience acquired worldwide in hadron therapy at the end of 2014 exceeds 118,000 patients and 15,000 patients for proton therapy and carbon therapy, respectively [41]. For example, current indications for protons and carbon ions include unresected or incompletely resected locally aggressive tumours located close to healthy critical structures, while paediatric malignancies that require improved tolerability of radiation are considered to be a priority for proton therapy. Detailed information can be found in recent articles and reviews [26].

5.1 Particle Type Selection

Although selection of the optimal type of ion remains a relevant topic of discussion, new facilities are now offering proton and carbon ions (for example, a manufacturer such as IBA, is developing hybrid systems), usually close to the photon therapy facility, raising the question of the preference of one type of particle over another. On the one hand, limited data are available concerning the toxicity of particle-based treatments and there is insufficient evidence to recommend the use of particles in many disease sites, making further clinical research programmes essential. On the other hand, reduction of the integral dose and increased RBE in the distal part of the physical dose distribution makes ion therapy highly attractive in challenging or radioresistant tumours. For example, in the case of skull base tumours, the overall conformality of combined photon-proton treatments has been discussed [18] to assess the clinical benefit of exclusive particle therapy. In the case of spinal locations, 3D conformal, IMRT, VMAT, tomotherapy and proton therapy have been compared in terms of dose escalation possibilities [77]. As discussed in Habrand 2009, the major advantage of proton therapy might concern paediatrics due to the potential for sparing normal tissues, but more clinical data and careful assessment of long-term side effects in children are needed. Prospective studies will inevitably be conducted, in parallel with optimization of dose delivery over time (dose escalations, hypofractionation), integration of particles into multimodal treatment and their implications on treatment planning.

5.2 Matching and Patching Fields

To improve conformality and reduce the dose to organs at risk, a dose delivery technique called "patching", specific to passive scattering in particle therapy, can be used. A multiple beam ballistic (usually two or three beams) is used to partially cover a complex shaped target volume while avoiding critical structures. In two-field patching, the beams are combined so that the distal edge of the first patch field is designed to stop on the lateral penumbra of the second through field (two typical examples are shown in Fig. 6). The distal fall-off of the first field and the lateral penumbra of the other field are matched to the 50 hot spots. However, the dose distribution along the patch junction is generally non-uniform because of tissue heterogeneities, heterogeneous dose gradients and a lack of analytical tools in treatment planning systems to take the scattering effects into account in the design of compensators. Therefore, patching and matching are always located within the target volumes, sometimes with small overshoots, as hot spots may not be detrimental if they are located within the target areas. To reduce the uncertainties, several patching fields are usually combined in order to create different shifted junctions that can be alternated every day and to minimize the dose delivered by each field.

5.3 Plan Review

Treatment planning review and assessment of doses distributions in proton or ion therapy use the same tools as in 3D conformal radiation therapy. For instance, many important parameters of an organ at risk or target volume dose distribution can

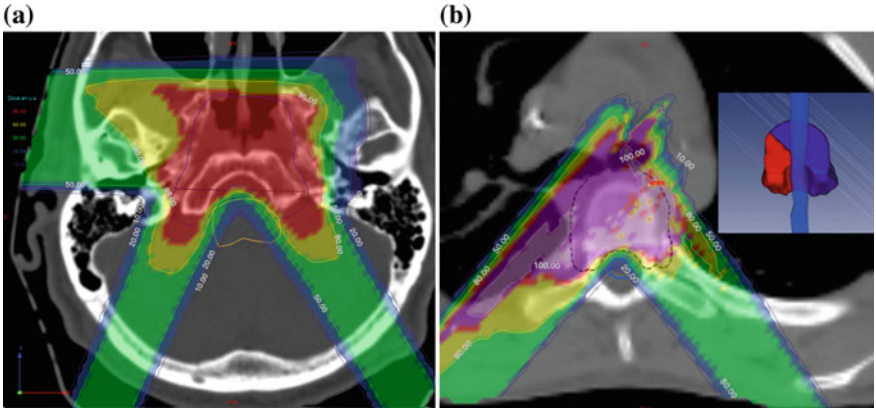

Fig. 6 Axial CT images with dose display in percent for typical chordoma cases, with a combination of patch/through fields: **a** three fields which irradiate anterior and posterior portions of the target while avoiding brainstem, **b** two fields avoiding spinal cord

be evaluated by inspection of the cumulative dose-volume histogram (DVH). The probability of achieving tumour control (called tumour control probability TCP), or complications for healthy structures (called normal tissue complication probability NTCP) can be used to describe the dose–response relationships for normal tissues or targets, using sigmoid-shaped formulas. In particular, generalized equivalent uniform dose (gEUD) can be used as an input parameter for such probability models (Eq. 15). The gEUD, which measures the physical dose for non-uniformly irradiated structures, while taking into account a biological dose response, is given by:

$$gEUD = \left(\sum_i \left(v_i D_i^a \right) \right)^{\frac{1}{a}} \tag{15}$$

where v_i is the volume fraction of the dose bin corresponding to the dose D_i and a characterizes the dose response behaviour of the OAR.

gEUD, with a value expressed in Gray, provides a simple method to compare treatment plans from different optimization results, can be a better prognostic predictor for late effects than the mean or maximum doses usually considered and can be easily used to formulate objective functions for IMRT or IMPT optimization. For example, this concept has been applied to determine optimal parameters of a gEUD-based NTCP for a group of patients with long-term follow-up data after skull base proton therapy [12].

6 Protons and Ions: Similarities and Comparisons

Clinical experience with the various types of ions is limited and is now becoming overwhelmingly dominated by carbon ion therapy. A comparison between proton and carbon ion therapy has been proposed [78] that includes many aspects of therapy in practice. A few aspects are highlighted here.

For example, proton beams have a lower RBE (1.1) than carbon ions (1.5–4): the uncertainties in the RBE and actual dose calculations are smaller for protons, but the increased RBE in the Bragg peak of carbon ions may increase TCP for challenging tumours. The angular spread of charged particles and the lateral penumbras increase in both beam line and patient. However, the angular spread for heavy ions is much smaller than for protons or X-rays (particularly for high beam energies for which scattering can even be neglected in some dose calculations) and constitutes a particular advantage of heavy ions compared to other radiations. In addition, as multiple scattering in air is an important contributor to lateral penumbra, especially at low energies, the use of patient apertures (even with scanned beams) and minimization of the air-gap between the aperture (or if necessary the range-shifter) and the patient may be required to achieve best penumbras. The dose of secondary lighter fragments created by nuclear fragmentation in the case of heavy ions produces a tail (which

does not exist for protons) in the depth dose curve at large depths: this nuclear fragmentation must be modelled to obtain a sufficiently accurate model of RBE and dose distribution for spread-out Bragg peaks. Range straggling with depth is markedly reduced for carbon ions compared to protons: the distal fall-off is much smaller for carbons, thus potentially requiring the use of a ridge-filter to improve the flatness in the spread-out Bragg peak, taking into account the biologically effective dose.

7 Radioprotection, Neutron Contamination

The high energies of the primary beam (from several dozen to several hundred MeV) commonly used in particle therapy are able to generate secondary neutrons through nuclear reactions within the different beamline components and the patient himself. In addition, the TPS used in routine clinical practice do not take into account secondary neutrons when calculating doses from primary particles and do not consider the elevated biological effectiveness of secondary and scattered neutrons from the treatment head.

Dosimetric studies on neutron doses have shown that particle therapy, especially with scanning techniques, could possibly lead to a further reduction in second malignancies because of the following factors: higher conformality because of the much lower entrance dose and no exit dose, less neutron scatter and, in many cases, fewer beams are needed to achieve good dose conformation. However, these findings may vary according to the beam delivery technique. As reported by Zheng et al. [83], a similar behaviour of neutron dose equivalent dependence on patient-specific beam parameters is expected between passive scattering and uniform scanning proton delivery systems. The neutron dose equivalent per absorbed dose is also expected to be slightly lower for uniform scanning beams than for passive scattering beams. The contribution of secondary neutron is expected to be the lowest for pencil beam scanning techniques, due to the absence of scattering devices in the treatment nozzle, patient apertures or compensators [16]. In reality, these findings could be mitigated by the possibility of using a range-shifter and the recent reintroduction of shaping devices to improve lateral penumbra. After having precisely characterized the secondary neutron doses received by paediatric patients treated for intracranial tumours [62], some authors are now developing facility-specific analytical models that could replace time-consuming MC calculations to assess accurate doses to healthy organs [17]. Furthermore, comparisons of the neutron contamination between photon, proton and ion therapy (for passive and scanning techniques) have shown that the out-of-field dose from secondary neutrons was lowest for ions (protons followed by heavier ions) delivered by scanning, followed by passive modulation, and finally by high-energy IMRT photons [73].

8 Biological Modelling

The biological effect of a given dose distribution differs between protons and other light ions. A constant relative biological effectiveness (RBE) equal to 1.1 is usually assumed for protons, while the RBE for other light ions varies substantially and must be estimated by mathematical models. Consequently, the radiobiological response of cells to particle deliveries has been extensively studied and its dependence on dose/fraction, position in the irradiated volume, beam energy and tissue has been characterized. The fraction of surviving cells as a function of dose is usually described by the linear-quadratic model (Eq. 16), where α and β are the parameters of the model, associated with initial slope and curvature for a single dose D. As experimental observations indicate a linear trend at high doses, the model has been modified and extrapolated by a straight line at doses higher than a threshold D_t [2].

$$S = \begin{cases} \exp\left(-\alpha D - \beta D^2\right) & \text{for } D < D_t \\ \exp\left(-\alpha D_t - \beta D_t^2 - (\alpha + 2\beta D_t) \cdot (D - D_t)\right) & \text{for } D \geq D_t \end{cases} \tag{16}$$

The RBE is defined as the ratio of the doses required by two radiations to cause the same level of effect. At a certain particle dose D_P, the RBE can then be expressed (Eq. 17) as a function of the parameters α_X, β_X and α_P, β_P (X refers to the reference radiation while P refers to the ion radiation).

$$RBE(\alpha_X, \beta_X, \alpha_P, \beta_P, D_P) = \frac{\sqrt{\alpha_X^2 + 4\beta_X D_P(\alpha_P + \beta_P D_P)} - \alpha_X}{2\beta_X D_P} \tag{17}$$

8.1 Microdosimetry

Microdosimetry can be defined as the estimation of the energy probability distribution imparted in an irradiated volume of matter, whereas dosimetry is the estimation of the mean energy imparted at one point of an irradiated volume of matter. In particle therapy, the spatial distribution of energy depositions (linear energy transfer analogous) and the amount of energy deposited in a volume (dose analogous) influence the relative biological effectiveness of radiation and must be defined experimentally or theoretically. Depending on the application area (microscopic or macroscopic), different physical quantities (stochastic or mean values) are then essential to define the biophysical models of radiation effects. For example, the LET concept, based on a mean value, has been developed as an approximation of the energy transfer by charged particles. The lineal energy y and the (frequency or dose) mean lineal energy, being stochastic values, are microdosimetric quantities that are commonly used to estimate biological effectiveness on scales similar to a mammalian cell nucleus (see section *RBE modelling for ions*). As a detailed review of the radiobiological modelling based

on these concepts is beyond the scope of this chapter, only a few definitions and a brief summary of some recent improvements in the main models used in particle therapy will be presented in the next sections.

8.2 RBE Modelling for Protons

The use of a generic RBE of 1.1 at 2 Gy in clinical proton therapy appears to be reasonable in view of the lack of experimental data to define accurate RBE models and the lack of clear clinical evidence for RBE variations [54]. Experimental in vivo and clinical data have also shown that this generic RBE value seems to be appropriate. However, many authors have reported variations of the RBE with depth in the spread-out Bragg peak proton beams used for treatment [6, 11], as well as significant differences in the final range and linear energy transfer, which can modulate biological effectiveness [53]. Indeed, wide-angle proton-proton scattering, nuclear interactions, and internally or externally produced neutrons are part of the physical processes involved in proton therapy. Some of these physical processes are not completely modelled in dose calculations by treatment planning systems, mostly based on measured data and water equivalent approximations. To account for this variable RBE in treatment planning, a few RBE models have been specifically developed for proton beams.

8.2.1 Definitions

Based on the observations that the maximum RBE for proton beams is observed at LET values around 30 keV/μm and that high LET values are of little practical relevance in clinical proton therapy, most biophysical models for the prediction of the RBE have been developed by assuming a linear relationship between RBE and LET. A few common definitions are provided below.

The dose-averaged LET (LET_d) distributions can easily be obtained from Monte Carlo simulations (Eq. 18) as a function of local particle spectrum and stopping power S taking into account primary particles, or from analytical calculations (Eq. 19) as a function of the mean stopping power:

$$LET_d(z) = \frac{\int_0^\infty \varphi_E(z) S^2(E) dE}{\int_0^\infty \varphi_E(z) S(E) dE} \tag{18}$$

where φ_E is the local particle spectrum at depth z with energies ranging between E et $E + dE$.

$$LET_d(z) = \frac{\langle S(z)^2 \rangle}{\langle S(z) \rangle} \tag{19}$$

where $\langle S(z) \rangle$ is the mean stopping power at depth z.

The absorbed dose D (or energy imparted per unit mass) can be expressed as a function of the beam fluency and LET (Eq. 20):

$$D = 1.6 \times 10^{-5} \times \Phi \times \frac{LET}{\rho} \tag{20}$$

with D in Gy, σn cm^{-2}, LET in keV/μm, and ρ the mass density in g/cm^3.

For example, assuming a 0.5 keV/μm LET value for a 200 MeV proton beam, the fluency to deposit 1 Gy in water would be 1.25 Gp/cm^2, (i.e. 12 $p/\mu m^2$). This means that a cell nucleus (≈5 μm diameter) would be crossed by 235 particles, each 0.25 μm apart. For alpha particles or gamma rays, this value would vary between a few tracks and a thousand tracks, respectively.

8.2.2 LET-RBE Models

The RBE can then be obtained by several parameterization as a function of LET, dose and tissue-specific parameters α/β, s described below:

- For one selected type of cells and a LET less than several dozen keV/μm (Eq. 21, [81], Eq. 22, [10]), the following two approximations have been proposed:

$$\alpha_P(LET) = \alpha_0 + \lambda LET \tag{21}$$

or

$$\alpha_P(LET) = \alpha_0 + \frac{1 - e^{-\lambda_1 . LET^2}}{\lambda_2} \tag{22}$$

(α_0 and λ_i have to be fitted to the experimental data for the tissue considered).
To ensure equality between low LET protons (≈0.5 keV/μm) and photons, as frequently observed experimentally, the following assumption can be adopted (Eq. 23):

$$\alpha_0 = \alpha_X - 0.5.\lambda \tag{23}$$

- Fits to a dozen cell lines result in the following two parameterizations of the previous linear relationship (Eq. 24, [79], Eq. 25, [8]):

$$\alpha_P(LET) = \alpha_X(1 + 0.434 \times \frac{\beta_X}{\alpha_X} \times LET) \tag{24}$$

or

$$\alpha_P(LET) = \alpha_X \left(0.843 + 0.154 \times 2.686 \times \frac{\beta_X}{\alpha_X} \times LET\right) \tag{25}$$

- In most of the literature, the quadratic parameter β is assumed to be constant ($\beta_P = \beta_X$) and LET-independent. However, several authors have shown experimentally that the β values for some cell lines appear to be LET-dependent. Therefore, one model (Eq. 26) explicitly assumes a dependency of β on LETand proposes a fit to experimental data (V79 Chinese hamster cells with mean $(\alpha/\beta)_X = 2.686$ Gy) of the behaviour of $\sqrt{(\beta_P/\beta_X)}$ as a function of LET [7, 8]:

$$\beta_P(LET) = \beta_X \left(1.09 + 0.006 \times 2.686 \times \frac{\beta_X}{\alpha_X} \times LET\right)^2 \tag{26}$$

An example of calculation of the RBE-weighted dose with the "Wedenberg" parameterization for a spread-out Bragg peak is given in Fig. 7.

8.3 RBE Modelling for Ions

The complex dependencies of the RBE for ions (with depth in tissue, applied dose, cell type, biological endpoint, particle type) have led to the development of several models to estimate RBE. Two main radiobiological models have been proposed, based on different physical and biological models already integrated into existing TPS (not yet used in France except for research purposes): the first one is used in

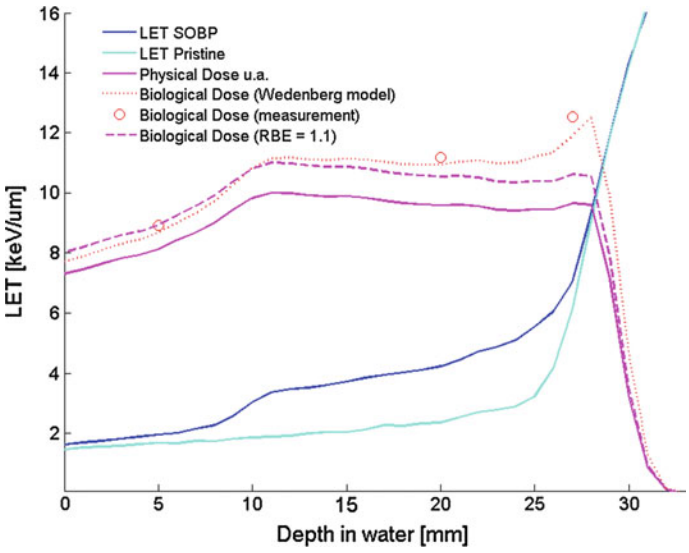

Fig. 7 Comparison of simulated LET_d, measured (*circle*) and calculated (*dotted* and *dashed lines*) RBE-weighted dose (for D37 endpoint, HeLa cells) of 58 MeV proton beams

Japan (HIMAC, NIRS) and is based on the microdosimetric kinetic model (MKM) developed by Hawkins [27–29], whereas the second model is used in Germany (GSI) and is based on the local effect model (LEM), now in its 5th version [67].

- The MKM combines assumptions from microdosimetry with kinetic relations for lethal lesions and sublethal lesions that are not repaired. Cell survival is then correlated with stochastic dose deposits in the volume of a small sensitive site (called domain with diameter $d < 1\,\mu m$) within the cell nucleus.

$$\alpha_P(E) = \alpha_0 + \beta_X \times \frac{4\bar{y}_d(E)}{\pi d^2} \tag{27}$$

  In Eq. 27, the term $\frac{4\bar{y}_d(E)}{\pi d^2}$ stands for an approximation of the mean specific energy deposited by a single event in a spherical domain composed of water, and is calculated from the mean lineal energy y_d. For high LET (above 100 keV/μm), the mean lineal energy is usually corrected for a saturation effect of the RBE. In practice, and according to the *Wilkens* model (Eq. 21), α_0 and β_x are independent of the radiation quality and equal to the cell-line parameters in the limit of zero LET.
- The LEM relates the response of biological systems after ion irradiation to the response after X-ray irradiation, and uses a parameterized dose-response curve derived from experimental photon data. It assumes that the biological effect of irradiation is determined by the spatial dose distribution inside the volume of a small sensitive site within the cell nucleus (nm scale as compared to the μm scale of MKM). By doing so, it also takes into account the biological effectiveness of the various nuclear fragments. LEM has been further improved to take into account clustered DNA damage [15].

9 Conclusions

In this chapter, we have provided an overview of the treatment planning procedure in proton and particle therapy. The main advantages and uncertainties of the current delivery systems have been described and, in particular, the special issues in planning for pencil beam scanning that are currently being addressed (multi-criteria optimization, sensitivity to delivery uncertainties, radiobiological effects that can be included in inverse optimization by LET calculations). The very promising results demonstrated with Monte Carlo codes (considered to be the most accurate methods to compute doses in radiation therapy) have led the community to evaluate fully integrated Monte Carlo dose calculations, which could also validate or be used for the commissioning and quality assurance of clinical beam delivery. In contrast with photons, protons and ions present the advantage of stopping at a given depth (at the site of the tumour) with reduced straggling, implying a significant reduction of integral dose to surrounding tissues. However, range uncertainties still represent one

of the major limitations to clinical application of the full potential of hadron therapy, and accurate modelling of relative biological effectiveness also remains highly challenging.

References

1. Andreo P (2009) On the clinical spatial resolution achievable with protons and heavier charged particle radiotherapy beams. Phys Med Biol 54(11):N205–N215
2. Astrahan M (2008) Some implications of linear-quadratic-linear radiation dose-response with regard to hypofractionation. Med Phys 35(9):4161–4173
3. Bert J et al (2013) Geant4-based Monte Carlo simulations on GPU for medical applications. Phys Med Biol 21;58(16):5593–5611
4. Bopp C et al (2015) Quantitative proton imaging from multiple physics processes: a proof of concept. Phys Med Biol 60:5325–5341
5. Bortfeld T (1997) An analytical approximation of the Bragg curve for therapeutic proton beams. Med Phys 24:2024–2033
6. Calugaru V et al (2011) Radiobiological characterization of two therapeutic proton beams with different initial energy spectra used at the Institut Curie Proton Therapy Center in Orsay. Int J Radiat Oncol Biol Phys 81(4):1136–1143
7. Carabe A et al (2007) The incorporation of the concept of minimum RBE (RBEmin) into the linear-quadratic model and the potential for improved radiobiological analysis of high-LET treatments. Int J Radiat Biol 83(1):27–39
8. Carabe A et al (2012) Range uncertainty in proton therapy due to variable biological effectiveness. Phys Med Biol 57:1159–1172
9. Chen W et al (2012) Including robustness in multi-criteria optimization for intensity-modulated proton therapy. Phys Med Biol 57:591–608
10. Chen Y et al (2012) Empirical model estimation of relative biological effectiveness for proton beam therapy. Radiat Protect Dosim 149(2):116–123
11. Courdi A et al (1994) The depth-dependent radiation response of human melanoma cells exposed to 65 MeV protons. Br J Radiol 67:800–804
12. Dedes G et al (2015) Monte Carlo study of the precision and accuracy of proton CT reconstructed relative stopping power maps. Med Phys 42:3298
13. De Marzi L et al (2013) Calibration of CT Hounsfield units for proton therapy treatment planning: use of kilovoltage and megavoltage images and comparison of parameterized methods. Phys Med Biol 58:4255–4276
14. De Marzi L et al (2015) Use of gEUD for predicting ear and pituitary gland damage following proton and photon radiation therapy. Br J Radiol 88:20140413
15. Elsässer T et al (2007) Cluster effects within the local effect model. Radiat Res 167:319–329
16. Farah J et al (2015) Measurement of stray radiation within a scanning proton therapy facility: EURADOS WG9 intercomparison exercise of active dosimetry systems. Med Phys 42(5):2572–84
17. Farah J et al (2015) Configuration and validation of an analytical model predicting secondary neutron radiation in proton therapy using Monte Carlo simulations and experimental measurements. Phys Med 31(3):248–256
18. Feuvret L et al (2007) A treatment planning comparison of combined photon-proton beams versus proton beams-only for the treatment of skull base tumors. Int J Radiat Oncol Biol Phys 69:944–954
19. Gottschalk B et al (1993) Multiple Coulomb scattering of 160 MeV protons. Nucl Instrum Methods Phys Res B 74:467–490
20. Gottschalk B et al (2015) On the nuclear halo of a proton pencil beam stopping in water. Phys Med Biol 60(2015):5627–5654

21. Grevillot L et al (2010) Optimization of GEANT4 settings for proton pencil beam scanning simulations using GATE. Nucl Instr Meth Phys Res B 268(20) 3295-3305
22. Grevillot L et al (2011) A Monte Carlo pencil beam scanning model for proton treatment plan simulation using GATE/GEANT4. Phys Med Biol 56:5203–5219
23. Grevillot L et al (2012) GATE as a GEANT4-based Monte Carlo platform for the evaluation of proton pencil beam scanning treatment plans. Phys Med Biol 57:4223–4244
24. Gueth P et al (2013) Machine learning-based patient specific prompt-gamma dose monitoring in proton therapy. Phys Med Biol 58(13):4563–4577
25. Habrand JL et al (2009) Proton beam therapy in pediatric radiotherapy. Cancer Radiother 13:550–5
26. Habrand JL et al (2013) Update of clinical programs using hadrontherapy 2008–2012. Cancer Radiother 17(5-6):400–406
27. Hawkins RB (1994) A statistical theory of cell killing by radiation of varying linear energy transfer. Radiat Res 140(3):366–374
28. Hawkins RB (1996) A microdosimetric-kinetic model of cell death from exposure to ionizing radiation of any LET, with experimental and clinical applications Int. J. Radiat. Biol. 69(6):739–755
29. Hawkins RB (2003) A microdosimetric-kinetic model for the effect of non-poisson distribution of lethal lesions on the variation of RBE with LET. Radiat Res 60(1):61–69
30. Hérault J et al (2005) Monte Carlo simulation of a protontherapy platform devoted to ocular melanoma. Med Phys 32(4):910–919
31. Hérault J et al (2007) Spread-out Bragg peak and monitor units calculation with the Monte Carlo code MCNPX. Med Phys 34(2):680–8
32. Highland VL (1975) Some practical remarks on multiple scattering. Nucl Instrum Methods 129:497–499
33. Hong L et al (1996) A pencil beam algorithm for proton dose calculations. Phys Med Biol 41:1305–1330
34. Inaniwa T (2014) Implementation of a triple Gaussian beam model with subdivision and redefinition against density heterogeneities in treatment planning for scanned carbon-ion radiotherapy. Phys Med Biol 59(18):5361–5386
35. Journal of the ICRU 2007 Vol. 7 No 2 Report 78
36. Jackson DF et al (1981) X-ray coefficients of elements and mixture. Phys Rep 70:169–223
37. Jan S et al (2004) GATE: a simulation toolkit for PET and SPECT. Phys Med Biol 49:4543–4561
38. Jan S et al (2011) GATE V6: a major enhancement of the GATE simulation platform enabling modelling of CT and radiotherapy. Phys Med Biol 56:881–901
39. Jan S et al (2013) GATE simulation of 12C hadrontherapy treatment combined with a PET imaging system for dose monitoring: a feasibility study. IEEE Trans Nucl Sci 60(1 part2):423–429
40. Jiang HY et al (2007) Effects of Hounsfield number conversion on CT based proton Monte Carlo dose calculations. Med Phys 34(4):1439–1449
41. Jermann M (2015) Particle therapy statistics in 2014. Int J Particle Ther 2(1):50–54
42. Lee M (1993) An empirical method to build up a model of proton dose distribution for a radiotherapy treatment-planning package. Phys Med Biol 38:989–998
43. Lestand L et al (2012) In-beam quality assurance using induced β+ activity in hadrontherapy: a preliminary physical requirements study using Geant4. Phys Med Biol 57:6497–6518
44. Lomax AJ (1999) Intensity modulated methods for proton therapy. Phys Med Biol 44:185–205
45. Lomax AJ et al (2004) The clinical potential of intensity modulated proton therapy. Z Med Phys 14:147–52
46. Martínez-Rovira I et al (2015) Implementation of biological washout processes within GATE/Geant4-A Monte Carlo study in the case of carbon therapy treatments. Med Phys 42:1773
47. Mazal A et al (1997) Robots in high precision patient positioning for conformal radiotherapy World Congress on Medical Physics and Biomedical Engineering. Med Biol Eng Comput 35:824

48. McGowan SE et al (2013) Treatment planning optimisation in proton therapy. Br J Radiol 86:20120288
49. Mustapha AA et al (1983) The relation between X-ray CT numbers and charged particles stopping powers and its significance for radiotherapy treatment planning. Phys Med Biol 28:169–176
50. Nauraye C et al (1995) An experimental approach to the design of a scattering system for a proton therapy beam line dedicated to ophthalmological applications. Int J Radiat Oncol Biol Phys 32(4):1177–1183
51. Oozeer R (1997) A model for the lateral penumbra in water of a 200-MeV proton beam devoted to clinical applications. Med Phys 24(10):1599–1604
52. Paganetti H (2005) Interpretation of proton relative biological effectiveness using lesion induction, lesion repair and cellular dose distribution. Med Phys 32:2548–2556
53. Paganetti H (2012) Range uncertainties in proton therapy and the role of Monte Carlo simulations. Phys Med Biol 57:R99–117
54. Paganetti H (2014) Relative biological effectiveness (RBE) values for proton beam therapy. Variations as a function of biological endpoint, dose, and linear energy transfer. Phys Med Biol 59:R419–R472
55. Pedroni E et al (2005) Experimental characterization and physical modelling of the dose distribution of scanned proton pencil beams. Phys Med Biol 50:541–561
56. Peucelle C et al (2015) Exploring new paths in particle therapy: a Monte Carlo study on the use of spatial fractionation of the dose. Physica Medica 30(Supplement 1):e27
57. Rit S et al (2013) Filtered backprojection proton CT reconstruction along most likely paths. Med Phys 40:031103
58. Robert C et al (2013) Distributions of secondary particles in proton and carbon-ion therapy: a comparison between GATE/Geant4 and FLUKA Monte Carlo codes. Phys Med Biol 58:2879–2900
59. Salvat F et al (2006) PENELOPE-2006, a code system for Monte Carlo simulation of electron and photon transport OECD, Spain. ISBN 92-64-02301-1
60. Sarrut D et al (2014) A review of the use and potential of the GATE Monte Carlo code for radiation therapy and dosimetry applications. Med Phys 41:064301
61. Sayah R et al (2013) Monte Carlo simulation of a proton therapy beamline for intracranial treatments. Radioprotection 48:317–339
62. Sayah R et al (2014) Secondary neutron doses received by paediatric patients during intracranial proton therapy treatments. J Radiol Prot 34(2):279–296
63. Schaffner B et al (1998) The precision of proton range calculations in proton radiotherapy treatment planning: experimental verification of the relation between ct-hu and proton stopping power. Phys Med Biol 43(6):1579–1592
64. Schaffner B (2008) Proton dose calculation based on in-air fluence measurements. Phys Med Biol 53:1545–1562
65. Schneider U et al (1996) The calibration of CT Hounsfield units for radiotherapy treatment planning. Phys Med Biol 41(1):111–124
66. Schneider W et al (2000) Correlation between CT numbers and tissue parameters needed for Monte Carlo simulations of clinical dose distributions. Phys Med Biol 45:459–478
67. Scholz M et al (1996) Track structure and the calculation of biological effects of heavy charged particles. Adv Space Res 18:5–14
68. Schwaab J et al (2011) Experimental characterization of lateral profiles of scanned proton and carbon ion pencil beams for improved beam models in ion therapy treatment planning. Phys Med Biol 56:7813–7827
69. Soukup M et al (2005) A pencil beam algorithm for intensity modulated proton therapy derived from Monte Carlo simulations. Phys Med Biol 50:5089–5104
70. Stankovskiy A et al (2009) Monte Carlo modelling of the treatment line of the Proton Therapy Center in Orsay. Phys Med Biol 54(8):2377–2394
71. Szymanowski H et al (2001) Experimental determination and verification of the parameters used in a proton pencil beam algorithm. Med Phys 28(6):975–987

72. Szymanowski H et al (2002) Two-dimensional pencil beam scaling: an improved proton dose algorithm for heterogeneous media Phys. Med Biol 47:3313–3330
73. Tessa CL et al (2014) Characterization of the secondary neutron field produced during treatment of an anthropomorphic phantom with x-rays, protons and carbon ions. Phys Med Biol 59(8):2111–2125
74. Ulmer W (2007) Theoretical aspects of energy-range relations, stopping power and energy straggling of protons. Radiat Phys Chem 76:1089–1107
75. Unkelbach J et al (2009) Reducing the sensitivity of IMPT treatment plans to setup errors and range uncertainties via probabilistic treatment planning. Med Phys 36:149–163
76. Vanderstraeten B et al (2007) Conversion of CT numbers into tissue parameters for Monte Carlo dose calculations: a multi-centre study. Phys Med Biol 52(3):539–562
77. Vogin G et al (2013) Localized Ewing sarcoma of the spine: a preliminary dose-escalation study comparing innovative radiation techniques in a single patient. Cancer Radiother 17(1):26–33
78. Weber U (2009) Comparison of carbon ions versus protons. Cancer J 15(4):325–332
79. Wedenberg M et al (2013) A model for the relative biological effectiveness of protons: The tissue specific parameter α/β of photons is a predictor for the sensitivity to LET changes. Acta Oncologica 52:580–588
80. Westerly DC et al (2013) A generalized 2D pencil beam scaling algorithm for proton dose calculation in heterogeneous slab geometries. Med Phys 40(6):061706
81. Wilkens JJ et al (2004) A phenomenological model for the relative biological effectiveness in therapeutic proton beams. Phys Med Biol 49:2811–2825
82. Zhang X et al (2011) Parameterization of multiple Bragg curves for scanning proton beams using simultaneous fitting of multiple curves. Phys Med Biol 56:7725–7735
83. Zheng Y et al (2012) Measurements of neutron dose equivalent for a proton therapy center using uniform scanning proton beams. Med Phys 39(6):3484–3492